CrystEngComm

Cite this: *CrystEngComm*, 2011, **13**, 5226

www.rsc.org/crystengcomm

PAPER

Hybrid dandelion-like $YH(O_3PC_6H_5)_2$:Ln (Ln = Eu^{3+}, Tb^{3+}) particles: formation mechanism, thermal and photoluminescence properties

Weihua Di,*[ab] Xinguang Ren,[c] Naoto Shirahata,[bd] Chunxu Liu,[c] Ligong Zhang,[c] Yoshio Sakka*[ab] and Nicola Pinna[ef]

Received 26th October 2010, Accepted 3rd May 2011
DOI: 10.1039/c1ce05473b

Lanthanide (Ln)-doped yttrium phenylphosphonate nanohybrids with an ordered dandelion-like morphology were synthesized by a simple citric acid-assisted hydrothermal process. The crystal structure, morphology and composition of the as-synthesized products were characterized by X-ray diffraction (XRD), scanning electron microscopy (SEM), transmission electron microscopy (TEM), Fourier transform infrared (FT-IR) spectroscopy and elemental analysis. The formation mechanism of self-assembled dandelion-like particles was demonstrated in detail on the basis of the morphological dependence of the as-synthesized products as a function of the concentration of the organic additive. Thermogravimetry/differential thermal analysis (TG/DTA) showed that the organic–inorganic hybrid structure is preserved until 450 °C, indicating the high thermal stability of the phenylphosphonate-based hybrids. Upon UV excitation, Ln (Eu^{3+}, Tb^{3+})-doped phenylphosphonate-based hybrids exhibit emission in the visible region due to an efficient energy transfer from phenyl rings to luminescent Ln centers. The photoluminescence characteristics of samples synthesized with and without citric acid were further quantified through the estimation of the absolute emission quantum yield. The maximum quantum yield value was attained for dandelion-shaped samples synthesized with citric acid, showing an increase of ~50% in comparison to that of the platelet-like sample synthesized without citric acid. This indicates that the photoluminescence properties can be improved by the tunable morphology.

1. Introduction

Hybrid materials with organic and inorganic building blocks uniformly distributed in the framework have attracted considerable attention in recent years because they connect organic and inorganic components at a molecular or nanometre level, generating new materials with novel properties.[1–7] Organic–inorganic hybrids combine the advantages of organic and inorganic compounds such as the functional versatility of organic chemistry, the easy processing of organic components, and the thermal and chemical stabilities of inorganic oxides.[8,9] Organic–inorganic hybrids are multifunctional materials offering desirable properties through the rational design of the compositions and structures of the organic and inorganic units. The emergence of hybrids has opened up an exciting direction of research in materials science and related technologies.[10]

Metal phosphonates are one type of organic–inorganic hybrid material, in which the phosphonate oxygens bond strongly to the metal ions, forming tightly bound inorganic lamellae. These inorganic layers can be built from planes of metal atoms with phosphonate groups lying above and below the plane.[11,12] The wide choice of metals and the versatility of organophosphorus molecules suggest the possibility of the rational design of structures and compositions. The interest in these hybrids originated from their versatile architectures and topologies, as well as their potential to form complex structures.[13] In particular, most metal phosphonate hybrids can exhibit porous structures. Clearfield's group has successfully synthesized a series of highly porous metal phosphonate hybrids that are highly stable up to 400 °C and also in acid media, and do not collapse when de-solvated.[14,15] These features indicate their promising applications in areas of technology including catalysts, sorbents, ion exchangers and intercalation chemistry.[16,17] Therefore, the research on

---

[a] *World Premier International Research (WPI), Center Initiative on Materials Nanoarchitronics (MANA), National Institute for Materials Science (NIMS), 1-2-1 Sengen, Tsukuba, Ibaraki, 305-0047, Japan. E-mail: DI.Weihua@nims.go.jp; SAKKA. Yoshio@nims.go.jp*
[b] *Advanced Ceramics Group, Advanced Materials Processing Unit, NIMS, 1-2-1 Sengen, Tsukuba, Ibaraki, 305-0047, Japan*
[c] *Key Laboratory of Excited-State Processes, Changchun Institute of Optics, Fine Mechanics and Physics, Chinese Academy of Sciences, 3888 Eastern South Lake Road, Changchun, 130033, People's Republic of China*
[d] *PRESTO, Japan Science and Technology Agency (JST), 4-1-8 Honcho Kawaguchi, Saitama, 332-0012, Japan*
[e] *Department of Chemistry, CICECO, University of Aveiro, 3810-193 Aveiro, Portugal*
[f] *World Class University (WCU) program of Chemical Convergence for Energy & Environment (C2E2), School of Chemical and Biological Engineering, College of Engineering, Seoul National University (SNU), Seoul, 151-744, Korea*

organophosphonate-based hybrids has focused mainly on the fabrication of micro-/mesoporous hybrid materials and characterizations related to the porous structures in recent years.[18–21]

Lanthanide (Ln)-doped organic–inorganic hybrids are an important family of materials since they exhibit unique luminescence properties with sharp and intense emission lines due to efficient intramolecular energy transfer from the coordinated ligands to the luminescent Ln centers (the antenna effect).[10,22–24] The global properties of luminescent Ln-doped hybrids can be well controlled and tuned by varying both the inorganic and organic components. Furthermore, they have high thermal and photochemical stabilities and good mechanical properties.[25] Therefore, they are expected to have applications in several fields of technology, including light-emitting and quantum-dot devices, active waveguides in the vis-IR spectral regions, active coatings, and bioanalytical and biomedical actuators and sensors.[10] The photoluminescence of Ln-doped phosphonate-based hybrids, including excited state lifetime, quantum efficiency and absolute emission quantum yield, has been seldom investigated. Especially, the absolute emission quantum yield is an important parameter of the luminescent material and is a quantitative characterization of the photoluminescence properties. However, the photoluminescence quantum yield of phosphonate-based hybrids has not been reported by other groups besides our recently published work.[26] Moreover, various reports, by other groups, on luminescent metal phosphonates focused only on the absorption and emission spectra.[27–29] Recently, we proved that phenylphosphonates can also be synthesized in non-aqueous media leading to a highly efficient lanthanide emission, but without a precise control of the size and morphology at the nanoscale.[26] In the present work it is demonstrated that the addition of organic additives in the aqueous synthesis leads to a good control of size and morphology at a nanoscale level. So, one of the purposes of this work is to investigate the size and morphological control, and the assembly behavior of phenylphosphonate-based hybrids. It is well known that the chemical and physical properties of functional materials consisting of either inorganic compounds or inorganic/organic hybrids are fundamentally related to their size, shape and dimensionality. So, rational control over these factors has become an important research issue in recent years. Among the various methods used, self-assembly of inorganic nanobuilding blocks into one-dimensional (1D), two-dimensional (2D), and three-dimensional (3D) ordered hierarchical superstructures is fascinating owing to their improved properties originating from their nanostructured building blocks and the manner in which they are organized. Although a wide variety of inorganic materials have been successfully prepared with complex hierarchical shapes by the solution-phase chemical method, the research on organic–inorganic hybrids constructed by self-assembly has been investigated to a less extent. Furthermore, the dependence of photoluminescence quantum yield as a function of the morphology of the material has not been reported, to the best of our knowledge.

In this work, a citric acid (CA)-mediated hydrothermal method was employed to synthesize Ln-doped yttrium phenylphosphonate ($YH(O_3PC_6H_5)_2$) with dandelion-like architectures. The CA molecule acts as the stabilizer and growth-directing agent to control the nucleation, growth and alignment of crystals, allowing the formation of 1D nanorods and their construction into an ordered dandelion-like aggregate. Upon UV excitation, Ln (Eu^{3+}, Tb^{3+})-doped phenylphosphonate-based hybrids exhibit visible emission due to an efficient energy transfer from phenyl rings to luminescent Ln centers. The photoluminescence quantum yield of samples depends on their morphologies. The highest quantum yield of 0.30 (Eu^{3+}) and 0.25 (Tb^{3+}) was attained for the dandelion-like aggregate. This indicates that the photoluminescence properties of materials can be tuned by tailoring their sizes and morphologies.

2. Experimental section

Synthesis

In the synthesis using CA ($CA/Y^{3+} = 2:1$) as a ligand, 20 mL of YCl_3 (0.2 M) solution was added to 20 mL of aqueous solution containing 8 mmol CA. The solution, which becomes turbid owing to the formation of a Y^{3+}–citrate complex, was continuously stirred vigorously at 60 °C for 30 min. Subsequently, 20 mL of aqueous solution containing 8 mmol of phenylphosphonic acid was added. After additional agitation for 15 min, the solution was transferred into a Teflon autoclave held in a stainless-steel autoclave. The autoclave was sealed and heated at 180 °C for 48 h. After cooling the autoclave to room temperature, the precipitate was separated by centrifugation, washed with deionized water and ethanol several times and finally dried overnight in air at 50 °C. Samples with different molar ratios of CA/Y^{3+} (1 : 0.5, 1 : 1) were synthesized by the same procedure, in which only the amount of CA was modified. For the synthesis without the CA ligand, 40 mL of aqueous solution of phenylphosphonic acid (0.2 M) was added directly to 20 mL of YCl_3 aqueous solution. The other preparation conditions and parameters were kept constant. Eu^{3+}- or Tb^{3+}-doped samples were synthesized under the same conditions by replacing a fraction of the YCl_3 with $Eu(NO_3)_3$ and $Tb(NO_3)_3$ ($Eu/(Eu + Y) = 5\%$ and $Tb/(Tb + Y) = 5\%$).

Characterization

X-Ray powder diffraction (XRD) data were collected on an X-ray diffraction analyzer (JDX-3500, JEOL Ltd, Japan; CuK_α X-radiation at 35 kV and 300 mA). The patterns were measured in the 2θ range from 3° to 60° with a scanning step of 0.02°.

The size and morphology of samples were investigated using a scanning electron microscope (SEM) (JSM-6500, JEOL) operating at 12 kV equipped with an energy-dispersive spectroscopy system. For the SEM observations, samples were prepared by adding one drop of the powder suspension in ethanol onto silicon. Transmission electron microscopy (TEM) investigations were carried using a JEOL 2200FS microscope. Samples for TEM observations were prepared by first dispersing the particles in ethanol with the assistance of ultrasonification and then adding one drop of the suspension onto a copper TEM grid coated with a holey carbon film.

Fourier transform infrared (FT-IR) spectra (Mattson 5000) of the samples were measured in the range of 4000–500 cm^{-1} in transmission mode. The pellets were prepared by adding 0.8 mg of the sample powder to 80 mg of KBr. The powders were mixed homogeneously and compressed at a pressure of 10 kPa to form transparent pellets.

Thermogravimetry and differential thermal analyses (TG and DTA) of the as-synthesized samples were performed using a thermoanalyzer (Thermo Plus TG 8120, Rigaku). The data were recorded at a scan rate of 10 °C min^{-1} from room temperature to 1100 °C in air.

The emission and excitation spectra were recorded at room temperature using a fluorescence spectrophotometer (F-7000, Hitachi). Fluorescent lifetime measurements were made under a pulsed excitation at 266 nm from the fourth harmonic of a Nd:YAG laser with a line width of 1.0 cm^{-1}, a pulse duration of 10 ns and a repetition frequency of 10 Hz. Absolute emission quantum yields were measured at room temperature using a quantum yield measurement system (C9920-02, Hamamatsu) with a 150 W xenon lamp coupled to a monochromator for wavelength discrimination, an integrating sphere as a sample chamber and a multichannel analyzer for signal detection. Three measurements were made for each sample and the average value was reported.

3. Results and discussion

Structure, morphology and composition

The yttrium phenylphosphonate organic–inorganic hybrids were synthesized *via* a simple hydrothermal process reacting yttrium chloride and phenylphosphonic acid with the assistance of CA. The reaction yield was as high as 95%, indicating the potential for large-scale production *via* a simple hydrothermal method. The size and shape of products were characterized by an electron microscopy (Fig. 1 and 2). The low-magnification scanning electron microscopy (SEM) image (Fig. 1(a)) shows that the as-synthesized products are composed of many dandelion-like superstructures with sizes in the range of 1–2 μm. The magnified SEM images (Fig. 1(b) and (c)) clearly reveal that each dandelion-shaped particle consists of numerous nanorods with a diameter of 60–80 nm and a length of 1 μm. Indeed, these nanorods are organized in a specific manner. It appears that these nanorods are radially grown at a center to form a spherical-shaped aggregate. Certainly, in some domains, we also observe the presence of hemisphere-like or plantain-like particles, as shown in Fig. 1(c). These aggregates are so stable that no separation or change was observed after they were subjected to sonication for 2 h (not shown).

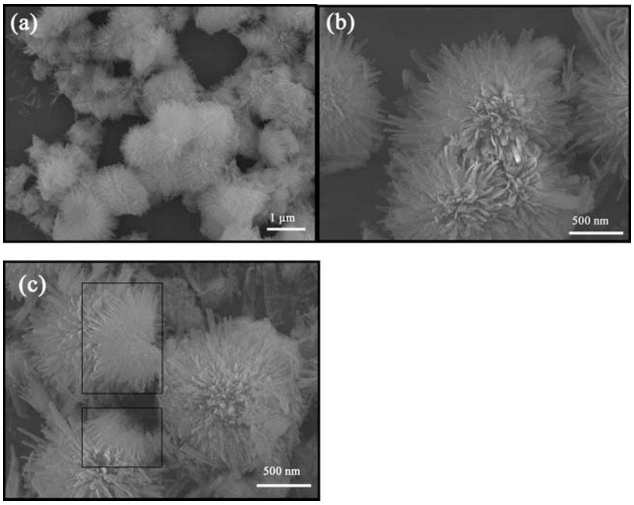

Fig. 1 Low (a) and high (b and c) magnification SEM images of as-synthesized products with CA as a ligand (CA : Y(III) = 2 : 1).

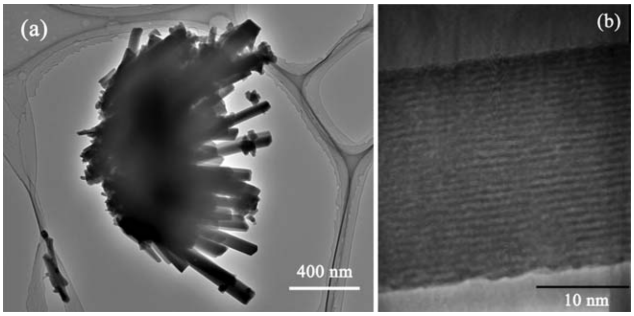

Fig. 2 Low (a) and high (b) magnification TEM images of as-synthesized products with CA as a ligand (CA : Y(III) = 2 : 1).

The morphology and microstructure of the as-synthesized products were further investigated in detail by TEM (Fig. 2). A representative TEM image of a randomly selected area shows that a single dandelion-shaped particle is composed of many nanorods radiating from their common bases (Fig. 2(a)), consistent with the SEM observations. The high-magnification TEM image (Fig. 2(b)) reveals that these nanorods are composed of equally spaced parallel lamellae with very different electron contrasts, demonstrating that the as-synthesized products have an organic–inorganic hybrid structure. The dark layers indicate the presence of strong scatterers, corresponding to the inorganic parts, whereas the organic materials between those inorganic layers are practically invisible. The interlayer distance calculated from the TEM image was about 1.55 nm. The organic–inorganic hybrid structure was also revealed by XRD analysis, as shown in Fig. 3(a). The most intense diffraction peak located at 5.8° is characteristic of a lamellar structure and corresponds to an interlamellar distance of about 1.55 nm, and hence to the (010) reflection of the lamellar structure reported by Wang *et al.*,[11] which is in good agreement with the interlamellar distance obtained by TEM. The second-, third- and fourth-order reflections are also observed at about 2θ = 11.7, 17.7 and 23.6°, respectively. The additional diffraction peaks were assigned to the inorganic rare earth phosphate and are in good agreement with the structure of lanthanum phenylphosphonate ($\mathrm{LaH(O_3PC_6H_5)_2}$) reported by Wang *et al.*[11] and our previous findings on various rare earth phenylphosphonates.[26]

The compositions of the as-synthesized yttrium phenylphosphonate hybrids were characterized by FT-IR spectroscopy, energy-dispersive X-ray spectrometry (EDX) and elemental analysis. The EDX spectrum shown in Fig. 3(b) reveals that the samples consist of C, P, O, Y and Eu (dopant). The presence of the Si peak is due to the silicon used as sample support for the measurement. The elemental analysis further quantifies the elemental components (mass %) of the as-synthesized products: Y, 20.1%; Eu, 1.9%; P, 15.2%; C, 36.2%; O, 24.1%, which correspond almost exactly to the values calculated from the chemical formula $\mathrm{YH(O_3PC_6H_5)_2}$:5%Eu: Y, 20.2%; Eu, 1.9%; P, 15.4%; C, 35.8%; O, 23.9%. These results indicate that Ln-doped $\mathrm{YH(O_3PC_6H_5)_2}$ has been synthesized successfully *via* a simple hydrothermal process.

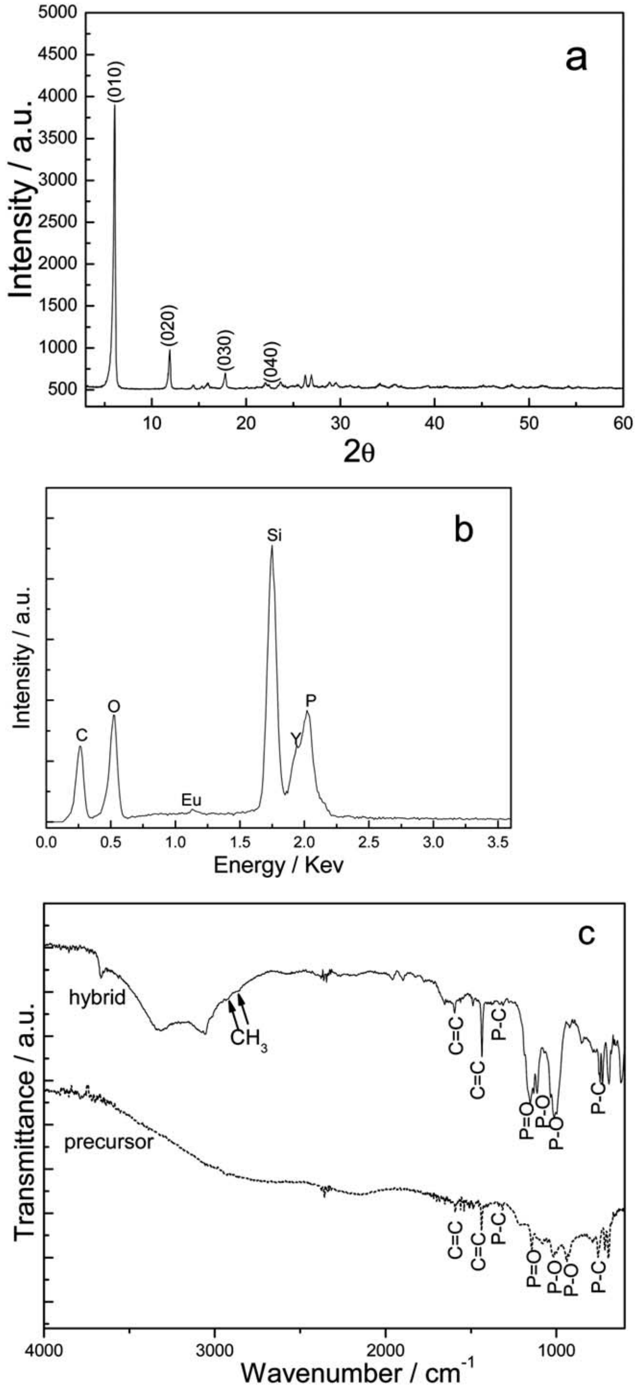

Fig. 3 XRD (a), EDX (b) and FT-IR (c) patterns of YH $(O_3PC_6H_5)_2$:0.05Eu. The dotted line in (c) represents the FTIR spectrum of the precursor (phenylphosphonic acid) for comparison.

The FT-IR spectrum provides further insight into the chemical composition of the as-synthesized products (Fig. 3(c)). The bands in the range 940–1140 cm^{-1} are ascribed to the different stretching vibrations of P–O groups,[30] and the peaks at approximately 1150 and 1165 cm^{-1} are characteristic of P=O vibrations.[31] The presence of the bands at approximately 750 and 1315 cm^{-1} is attributed to P–C stretching vibrations.[32] The peaks at about 1439 and 1486 cm^{-1} are related to the ν(C=C) vibrations resulting from the phenyl ring.[13] The bands around 3030 and 3665 cm^{-1} are due to the presence of hydroxyl groups coordinated to the phosphorus atom (P–OH).[33] These specific function groups are also found in the precursor (phenylphosphonic acid), only a slight shift of these functional group locations was observed (Fig. 3(c)). The low-intensity peaks at 2859 and 2920 cm^{-1} are ascribed to νs(CH_3) vibrations originating from the surface adsorption of citrate groups acting as ligands of Y^{3+} in the synthesis. The FT-IR results further confirm the formation of phenylphosphonate-based hybrid structures.

Possible growth mechanism

The shape of the as-synthesized product depends strongly on the concentration of CA added to the reaction system, as shown in Fig. 4. In the absence of CA, the products are mostly composed of platelet shaped inhomogeneous crystals (Fig. 4(a)). The platelet-like morphology has been frequently observed in the preparation of phosphonate-based layered hybrids.[14] Upon addition of CA to the reaction system, some nanorods start to appear in addition to the platelets (Fig. 4(b)). Upon further increasing the concentration of CA, a large number of nanorods are formed, and some of which aggregate into a well-defined dandelion-like or plantain-like shape (Fig. 4(c) and (d)).

The above observations suggest that CA plays a key role in the formation of nanorods and further construction of these nanorods into a dandelion-like shape. First, CA is a coordinating organic ligand with three –COOH groups and one –OH group,[34] and it is involved in the formation of Y^{3+}–citrate (Cit^{3-}) complexes through a strong coordination interaction with Y^{3+}. Such a complex is formed before phenylphosphonic acid is added to the reaction mixture.[33,34] Upon the addition of phenylphosphonic acid, phenylphosphonic groups compete with Cit^{3-} chelators. The initial formation of the Y^{3+}–citrate complex can obviously control the nucleation rate by reducing the rate of reaction. Second, the addition of CA strongly modifies the pH of the reaction system due to the deprotonation of the COOH groups of CA.[35] It was found that the pH values changed markedly from 6.0 to 2.5 as the concentration of CA added to YCl_3 aqueous solution was increased (the ratio CA/Y^{3+} was

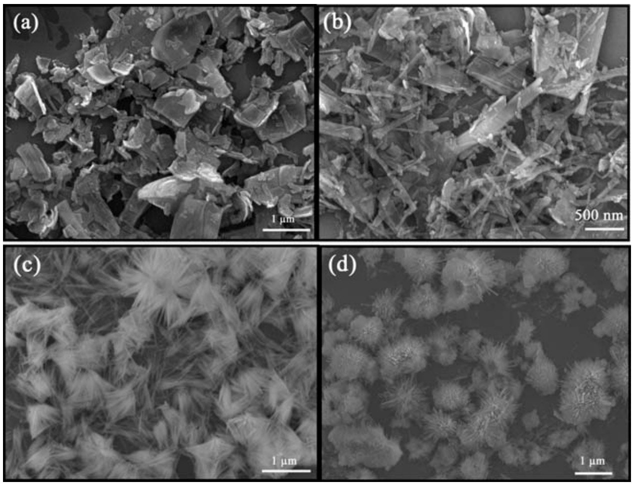

Fig. 4 SEM images of the as-synthesized samples: (a) without CA, (b) CA : Y = 0.5 : 1, (c) CA : Y = 1 : 1 and (d) CA : Y = 2 : 1.

changed from 0 : 1 to 2 : 1). It is well known that phenylphosphonic acid contains two hydroxyl groups coordinated to the phosphorus atom, and it can also exist in various protonated/deprotonated forms.[36] Clearly, the protonation/deprotonation equilibrium for phenylphosphonic acid is strongly dependent on the pH of the reaction solution. As a result, the rate of the release of $[C_6H_5PO_3H_{2-n}]^{n-}$ groups was well-adjusted through the pH of the reaction system, which is determined by the addition of different concentrations of CA. The controlled tunability of the release of $[C_6H_5PO_3H_{2-n}]^{n-}$ groups gives a subtle influence on the reaction rate of the Y^{3+}–Cit^{3-} complex with phenylphosphonic acid, enabling accurate control of the nucleation and growth of crystals. Third, organic additives are usually an effective shape modifier through their selective binding to specific crystallographic facets.[33,34,37] The preferable adsorption of citrate anions can modify the relative growth ratio of the crystallographic facets due to the relative change of surface energy. Therefore, one of the consequences of the presence of citrate anions is the inhibition of a certain growth directions and the relative enhancement of a specific growth direction, leading to the formation of one-dimensional nanorods. In our experiment, the effective control of nucleation rate and the selective adsorption of citrate groups on specific crystallographic facets in the presence of CA are thought to be responsible for the formation of homogeneous nanorods.

On the basis of the formation of these one-dimensional nanorods, the construction of dandelion-like aggregates can be understood as follows (see Scheme 1). There are spherical colloidal particles of a metal-containing precursor (metal–citrate complex) in the phosphonate solutions during the hydrothermal reaction. Nucleation should occur on the surface of these spherical particles. Since the crystal growth of one dimension for our hybrid materials is much faster than that of the other dimensions, rod-like crystals should radially grow from the surface of the particles to form dandelion-like morphology, where the central particles serve as glue. Therefore, the dandelion-like morphology should be a consequence of the radial growth of nano-sized rods at the colloidal spherical particles, as described in Scheme 1. If the metal source is consumed or crystal growth to non-radial directions proceeds, the spherical aggregates tend to break into hemispheres and smaller fragments, probably with plantain-like morphology, and finally to separate into independent nanorods. The formation of the plantain-like shape is also probably due to the fact that the growth of crystals starts from the region in contact to the Teflon bottle surface, which inhibits the radial growth of nanorods.

Thermal properties

To determine the thermal properties of the as-synthesized organic–inorganic hybrids, TG and DTA were carried out. TG/DTA curves of $YH(O_3PC_6H_5)_2$ are shown in Fig. 5. The observed weight loss occurs in four steps. The first weight loss at about 110 °C is due to the release of 2 wt% water molecules adsorbed onto the powder surface during the storage of the material in air. This was accompanied by an endothermic peak at about 120 °C, as shown in the DTA curve. The second weight loss starts at 235 °C and finishes at about 280 °C and is attributed to the release of water molecules formed by the condensation of two hydroxyl groups coordinated to the phosphorus atom (P–OH).[32] This is also accompanied by an endothermic peak with low intensity centered at 265 °C. The most significant weight loss occurs in the temperature range of 400–500 °C and is attributed to the decomposition and combustion of the organic moieties of the hybrid structures. Consequently, an exothermic peak can be observed in the DTA curve in this temperature range. This indicates the extremely high thermal stability of phenylphosphonate-based hybrids structure, which is retained up to 450 °C.[11,38] The weight loss of 23.5% associated with the combustion of organic moieties is lower than the total C and H contents obtained from the elemental analysis of $YH(O_3PC_6H_5)_2$. This is ascribed to incomplete combustion since we found that the residue of samples after TG/DTA measurement had high carbon content. The complete removal of the organic components requires heating for a longer time at a higher temperature.[11] Finally, a slight decrease in weight is observed from 800 °C up to more than 1000 °C. A crystallization process should be responsible for this weight loss. The residue of organic–inorganic hybrids after the removal of organic components contains compounds related to Y–PO_3. Further calcinations at a higher temperature lead to the conversion of Y–PO_3-related compound to crystalline YPO_4, which is accompanied by the volatilization of P_2O_5.[11] In the DTA curve, a typical wide endothermic band associated with crystallization can be clearly observed.

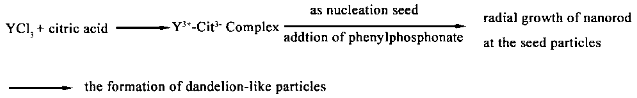

Scheme 1 Illustration for the formation process of the dandelion-like particles.

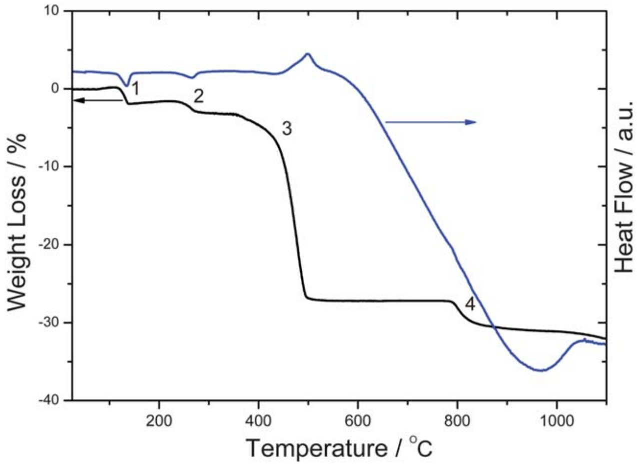

Fig. 5 TG/DTA curves of $YH(O_3PC_6H_5)_2$ hybrids.

Photoluminescence

Fig. 6 shows the excitation spectrum monitored within the $^5D_0 \rightarrow {}^7F_2$ transition (614 nm) for $YH(O_3PC_6H_5)_2$:0.05Eu hybrids. The spectrum consists of a broad band peaking at 272 nm, ascribed to the excited states of the phenyl rings of the phosphonates coordinated to the Eu^{3+} ions (this band is also

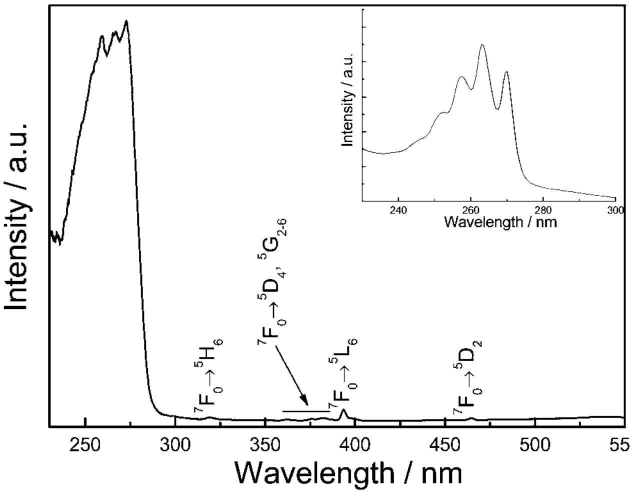

Fig. 6 Excitation spectrum of $YH(O_3PC_6H_5)_2$:0.05Eu monitored within the $^5D_0 \rightarrow {}^7F_2$ transition (614 nm). The inset shows the UV-Vis absorption of the same sample.

observed in the UV-vis absorption spectrum, inset of Fig. 6), as well as a series of lines ascribed to intra-4f^6 transitions of Eu^{3+} between the $^7F_{0,1}$ levels and the $^5H_6$, $^5D_{4-1}$, $^5G_{2-6}$ and $^5L_6$ excited states. The relatively high intensity of the broad band indicates that the Eu^{3+} ions are essentially populated *via* the excitation of the phenyl rings excited states.[26]

Fig. 7 shows high-resolution emission spectra of $YH(O_3PC_6H_5)_2$:0.05Eu with different excitation paths. An excitation into phenyl rings at 272 nm yields strong emission of Eu^{3+}, ascribed to the Eu^{3+} intra-4f^6 $^5D_0$–^7F_J (J = 0, 1, 2, 3, 4) transitions. Apart from the emission from Eu^{3+} intra-4f^6 transitions, no phenyl-related emission (see inset of Fig. 7) was observed, suggesting that the energy transfer from the phenyl group to Eu^{3+} is efficient. It is well known that the relative intensity of the $^5D_0$–$^7F_1$ transition (a typical magnetic dipole transition) and $^5D_0$–$^7F_2$ transition (a typical electric dipole transition) depends strongly on the local symmetry of Eu^{3+} ions.[39] When Eu^{3+} ions occupy an inversion center site, the $^5D_0$–$^7F_1$ transition should be relatively strong, while the $^5D_0$–$^7F_2$ transition is parity forbidden and should be very weak. For Eu^{3+}-doped $YH(O_3PC_6H_5)_2$, the relatively strong emission of Eu^{3+} $^5D_0$–$^7F_2$ transitions was observed, compared with that of $^5D_0$–$^7F_1$ transitions. It can be reasonably concluded that Eu^{3+} ions occupy a local site without inversion center symmetry in the hybrid $YH(O_3PC_6H_5)_2$ structure.

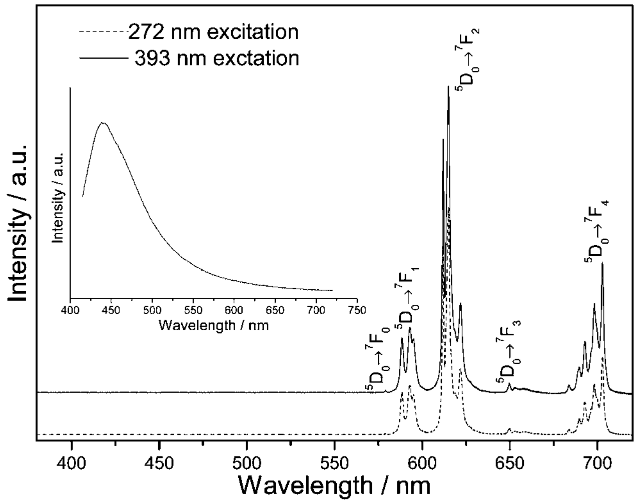

Fig. 7 High-resolution emission spectra of the $YH(O_3PC_6H_5)_2$:0.05Eu excited at 272 nm and 393 nm. The inset shows the emission spectrum of undoped $YH(O_3PC_6H_5)_2$.

Upon the direct excitation of Eu^{3+} at 393 nm, the same spectral lines were observed as those obtained upon the excitation of phenyl rings. This indicates that the energy, FWHM and the number of Stark components of the Eu^{3+} emission lines are independent of the excitation path (direct intra-4f^6 excitation or *via* the phenyl-related states), suggesting that all the Eu^{3+} ions occupy the same average local environment in the $YH(O_3PC_6H_5)_2$ hybrid structure.

Fig. 8(a) shows the excitation spectrum of $YH(O_3PC_6H_5)_2$:0.05Tb monitored within the $^5D_4$–$^7F_5$ transition (544 nm). A wide band is centered at 272 nm, which is also observed in the excitation spectrum of $YH(O_3PC_6H_5)_2$:0.05Eu (Fig. 6). This indicates that the excitation of Tb^{3+} is also generated *via* the sensitization of phenyl rings excited states, similarly to the case of the Eu^{3+} doped sample. The series of spectral lines in the range of 300–500 nm are ascribed to Tb^{3+} intra-4f^8 transitions between the $^7F_6$ level and the $^5L_{10-7}$, $^5G_{6-2}$ and $^5D_{4,2}$ excited states. The excitation of the phenyl rings at 272 nm yields strong emission ascribed to the Tb^{3+} intra-4f^8 $^5D_4$–$^7F_{6-3}$ electronic transitions (Fig. 8(b)). Similarly, we did not observe any phenyl-related emission, suggesting that the energy transfer from phenyl to Tb^{3+} is also efficient.

The fluorescence decay of $Eu^{3+}(^5D_0)$ and $Tb^{3+}(^5D_4)$ was measured at room temperature and is shown in Fig. 9(a) and (b), respectively. The fluorescent decay curves of Eu- and Tb-doped hybrids can be well fitted by a single-exponential function with lifetimes of 2.0 and 1.7 ms, respectively. The occurrence of single-exponential fluorescence decay further supports the conclusion that a single local environment for Ln^{3+} cations is present in the hybrid $YH(O_3PC_6H_5)_2$ structure.

The photoluminescence characteristics were further quantified through the estimation of the absolute emission quantum yield (QY). For all the samples, the maximum QY values were obtained at 272 nm excitation wavelength, confirming that the preferential path for the Eu^{3+} excitation is *via* the phenyls' excited state. To check the effect of the size and morphology on the photoluminescence performance, we compared the quantum yield of the samples with various morphologies, as listed in Table 1. The QY values of Eu- and Tb-doped dandelion-like samples show an increase of about 50%, compared to those of the platelet-like samples. This indicates that the photoluminescence properties can be improved by the tunable morphology due to the addition of CA. The origin of the morphological dependence of photoluminescence properties is not clear, and will require additional investigations. In a word, the phosphonate-based hybrids are promising functional materials due to high thermal stability and efficient photoluminescence. Moreover, due to the versatility of organophosphorus chemistry the modification of the organic part is facilitated with the selected organophosphorus molecule. This will certainly permit us to tailor the composition, morphology and the properties of the hybrid phosphonate materials.

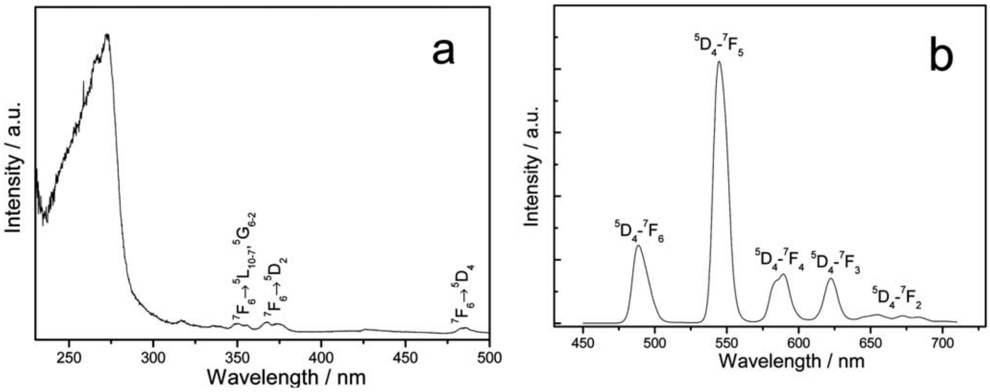

Fig. 8 Excitation (a) and emission (b) spectra of $YH(O_3PC_6H_5)_2$:0.05Tb.

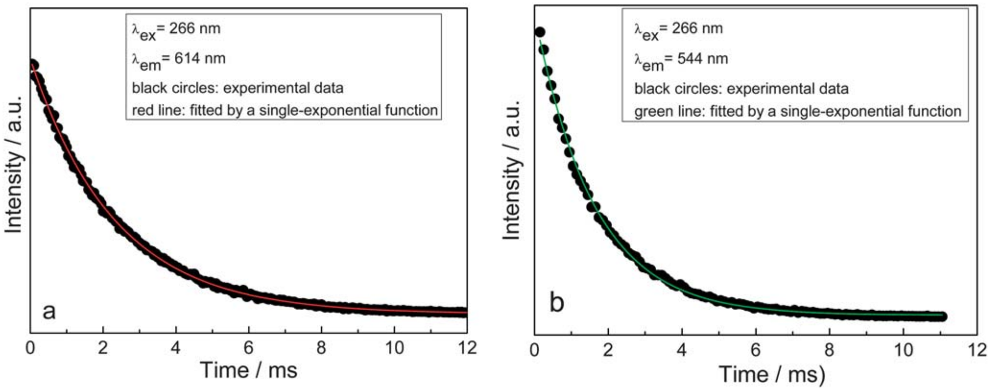

Fig. 9 Fluorescence decay of Eu^{3+}-doped (a) and Tb^{3+}-doped (b) $YH(O_3PC_6H_5)_2$.

Table 1 Absolute emission quantum yield of Eu- and Tb-doped $YH(O_3PC_6H_5)_2$ with various morphologies arising from various CA/Y^{3+} ratios

CA/Y^{3+} (molar ratio) morphologies	0 : 1 Platelet-like	0.5 : 1 Isolated nanorods	1 : 1 Plantain-like	2 : 1 Dandelion-like
$YH(O_3PC_6H_5)_2$: Eu	0.19	0.17	0.24	0.30
$YH(O_3PC_6H_5)_2$: Tb	0.16	0.17	0.22	0.25

4. Conclusions

Lanthanide (Ln)-doped yttrium phenylphosphonate hybrids with dandelion-like morphology were synthesized by a simple citric acid-assisted hydrothermal process. XRD and TEM studies revealed that the inorganic units (lanthanide phosphate) are separated by organic units (phenyl rings) to form ordered lamellar structures. Citric acid plays multiple roles in controlling the crystal growth and the formation of well-defined 3D architecture. The phenylphosphonate-based hybrid nanostructure is stable up to 450 °C. An efficient energy transfer from phenyl rings to luminescent Ln centers leads to an intense red (Eu^{3+}) or green (Tb^{3+}) emission. The absolute emission quantum yield of the as-synthesized hybrids shows a dependence on the morphology. The maximum quantum yield was attained for the sample with a dandelion-like superstructure, compared with that of other samples with different morphologies. In this work, not only the formation of phosphonate-based nanohybrids into an ordered 3D architecture was demonstrated, but it also turns out that the photoluminescence performance of materials is closely related to their size, shape and dimensionality.

Due to the versatility of organophosphorus chemistry, the modification of the organic component is easily achievable. This will certainly permit us to tailor the composition, morphology and the properties of the hybrid phosphonate materials. In addition, the emitted color of hybrid materials can be tuned from the visible to IR through selective doping of lanthanide ions (*e.g.* Tb, Eu, Yb/Er) or transition metal cation (*e.g.* Mn) due to an efficient intramolecular energy transfer from the organophosphorus component to the luminescent Ln centers (antenna effect). This fully shows attractive perspective of hybrid phosphonate-based materials.

Acknowledgements

This study was partly supported by a Grant-in-Aid for Scientific Research from the JSPS and the World Premier International Research (WPI) Center Initiative on Materials Nanoarchitronics (MANA), MEXT, Japan, the WCU (World Class University) program through the National Research Foundation of Korea funded by the Ministry of Education, Science and Technology (R31-10013) and FCT project (PTDC/CTM/73243/2006). NS wishes to thank the JST PRESTO program for financial support.

References

1 C. J. Brinker and G. W. Scherer, *Sol–Gel Science: the Physics and Chemistry of Sol–Gel Processing*, Academic Press, San Diego, USA, 1990.
2 P. Judeinstein and C. Sanchez, *J. Mater. Chem.*, 1996, **6**, 511.
3 P. N. Minoofar, R. Hernandez, S. Chia, B. Dunn, J. I. Zink and A. C. Franville, *J. Am. Chem. Soc.*, 2002, **124**, 14388.
4 R. Ganesan and A. Gedanken, *Nanotechnology*, 2008, **19**, 435709.
5 J. L. Chavez, H. Jiang and R. S. Duran, *Nanotechnology*, 2010, **21**, 055703.
6 M. S. Chen, C. S. Dulcey, L. A. Chrisey and W. J. Dressick, *Adv. Funct. Mater.*, 2006, **16**, 774.
7 S. L. Brandow, M. S. Chen, C. S. Dulcey and W. J. Dressick, *Langmuir*, 2008, **24**, 3888.
8 C. Molina, K. Dahmouche, C. V. Santilli, A. F. Craievich and S. J. L. Ribeiro, *Chem. Mater.*, 2001, **13**, 2818.
9 J. L. Liu and B. Yan, *J. Phys. Chem. B*, 2008, **112**, 10898.
10 L. D. Carlos, R. A. S. Ferreira, V. de Zea Bermudez and S. J. L. Ribeiro, *Adv. Mater.*, 2009, **21**, 509.
11 R. Wang, Y. Zhang, H. Hu, R. R. Rrausto and A. Clearfield, *Chem. Mater.*, 1992, **4**, 864.
12 A. Cabeza, M. Aranda, S. Bruque, D. Poojary, A. Clearfield and J. Sanz, *Inorg. Chem.*, 1998, **37**, 4168.
13 I. L. V. Rosa, A. V. S. Lourenco and C. R. J. Neri, *J. Fluoresc.*, 2006, **16**, 455.
14 A. Clearfield, *Dalton Trans.*, 2008, 6089.
15 M. D. Gomez-Alcantara, A. Cabeza, L. Moreno-Real, M. A. G. Aranda and A. Clearfield, *Microporous Mesoporous Mater.*, 2006, **88**, 293.
16 A. Subbiah, D. Pyle, A. Rowland, J. Huang, R. A. Narayanan, P. Thiyagarajan, J. Zon and A. Clearfield, *J. Am. Chem. Soc.*, 2005, **127**, 10826.
17 K. Maeda, *Microporous Mesoporous Mater.*, 2004, **73**, 47–55.
18 T. Kimura, *Chem. Mater.*, 2005, **17**, 5521–5528.
19 T. Y. Ma, X. J. Zhang, G. S. Shao, J. L. Cao and Z. Y. Yuan, *J. Phys. Chem. C*, 2008, **112**, 3090.
20 S. Yoo, D. Ford and F. Shantz, *Langmuir*, 2006, **22**, 1839.
21 M. Sakurai, A. Shimojima, M. Heishi and K. Kuroda, *Langmuir*, 2007, **23**, 10788.
22 N. Sabbatini, M. Guardingli and J. M. Lehn, *Coord. Chem. Rev.*, 1993, **123**, 201.
23 J. H. Park, J. Y. Kim, B. D. Chin, Y. C. Kim, J. K. Kim and O. O. Park, *Nanotechnology*, 2004, **15**, 1217.
24 N. Pinna, *J. Mater. Chem.*, 2007, **17**, 2769.
25 T. Kishida, N. Fujita, K. Sada and S. Shinkai, *Langmuir*, 2005, **21**, 9432.
26 W. H. Di, R. A. S. Ferreira, M. G. Willinger, X. G. Ren and N. Pinna, *J. Phys. Chem. C*, 2010, **114**, 6290.
27 R. Singleton, J. Bye, J. Dyson, G. Baker, R. Ranson and G. Hix, *Dalton Trans.*, 2010, **39**, 6024.
28 J. Rueff, N. Barrier, S. Boudin, V. Dorcet, V. Caignaert, P. Boullay, G. Hix and P. Jaffres, *Dalton Trans.*, 2009, 10614.
29 L. L. Gao, S. Y. Song, J. F. Ma and J. Yang, *Cryst. Growth Des.*, 2007, **7**, 895; S. Y. Song, J. F. Ma, J. Yang, M. H. Cao, H. J. Zhang, H. S. Wang and K. Y. Yang, *Inorg. Chem.*, 2006, **45**, 1201.
30 W. H. Di, X. X. Zhao, S. Z. Lu, X. J. Wang and H. F. Zhao, *J. Solid State Chem.*, 2007, **180**, 2478.
31 A. M. Botelho do Rego, A. M. Ferraria, J. E. Beghdadi, F. Debontridder, P. Brogueira, R. Naaman and M. Rei Vilar, *Inorg. Chem.*, 2005, **21**, 8765.
32 Y. G. Guo, S. F. Tang, B. P. Yang and J. G. Mao, *J. Solid State Chem.*, 2008, **181**, 2713.
33 W. H. Di, M. G. Willinger, R. A. S. Ferreira, X. G. Ren, S. Z. Lu and N. Pinna, *J. Phys. Chem. C*, 2008, **112**, 18815.
34 C. X. Li, Z. Y. Hou, C. M. Zhang, P. P. Yang, G. G. Li, Z. H. Xu, Y. Fan and J. Lin, *Chem. Mater.*, 2009, **21**, 4598.
35 S. Cho, J. W. Jang, S. H. Jung, B. R. Lee, E. Oh and K. H. Lee, *Langmuir*, 2009, **25**, 3825.
36 T. Uchikoshi and Y. Sakka, *J. Am. Ceram. Soc.*, 2008, **91**, 1923.
37 R. C. Jin, Y. C. Cao, E. C. Hao, G. S. Metraux, G. C. Schatz and C. A. Mirkin, *Nature*, 2003, **425**, 487.
38 G. Alberti, U. Costantino, S. Allulli and N. Tomassini, *J. Inorg. Nucl. Chem.*, 1978, **40**, 1113.
39 B. R. Judd, *Phys. Rev.*, 1962, **127**, 750.